Non-invasive optical guided tumor metastasis/vessel imaging by using lanthanide nanoprobe with enhanced down-shifting emission beyond 1500 nm

Youbin Li [†], *Songjun Zeng* [†]*, *Jianhua Hao* [‡]*

[†]Synergetic Innovation Center for Quantum Effects and Application, Key Laboratory of Low-dimensional Quantum Structures and Quantum Control of Ministry of Education, School of Physics and Electronics, Hunan Normal University, Changsha, 410081, P.R. China.

[‡]Department of Applied Physics, The Hong Kong Polytechnic University, Hong Kong, China.

ABSTRACT: Visualization of tumor vessels/metastasis and cerebrovascular architecture is vital important for analyzing pathological states of brain diseases and tumor's abnormal blood vessel to improve cancer diagnosis. *In vivo* fluorescence imaging using second near infrared emission beyond 1500 nm (NIR-IIb) is emerged as a next generation optical imaging method with significant improvement in imaging sensitivity and spatial resolution. Unfortunately, highly biocompatible probe capable of generating NIR-IIb emission with sufficient brightness and uniformed size is still scarce. Here, we have proposed the polyacrylic acid (PAA)-modified $NaLnF_4$:40Gd/20Yb/2Er nanorods (Ln=Y, Yb, Lu, PAA-Ln-NRs) with enhanced downshifting NIR-IIb emission, high quantum yield (QY), relative narrow bandwidth (~160 nm) and high bio-compatibility *via* Ce^{3+} doping for high performance NIR-IIb bioimaging. The downshifting emission beyond 1500 nm is improved by 1.75~2.2 times with simultaneously suppressing the upconversion (UC) path in Y, Yb, and Lu hosts *via* Ce^{3+} doping. Moreover, compared with the traditionally used Y-based host, the QY of NIR-IIb emission in Lu-based probe in water is improved from 2.2% to 3.6%. The explored bright NIR-IIb emitted PAA-Lu-NRs were used for high sensitivity small tumor (~ 4 mm)/metastatic tiny tumor detection (~ 3 mm), tumor vessel visualization with high spatial resolution (41 μm) and brain vessel imaging. Therefore, our findings open up the opportunity of utilizing lanthanide based NIR-IIb probe with bright 1525 nm emission for *in vivo* optical-guided tumor vessel/metastasis and non-invasive brain vascular imaging.

KEYWORDS: rare-earth nanoprobes, enhancement of downshifting emission, tiny metastatic tumor detection, tumor vascular imaging.

Cerebrovascular disorders and cancer are a major cause of death, devastating morbidity, and long-term disabilities in humans.[1-8] In the past decades, non-invasive brain/tumor vascular and metastasis tumor imaging were emerged as indispensible technique for the identification of cerebrovascular anomalies and tumor-associated vascular features.[1-4,7,8] Current vascular imaging techniques including X-ray computed tomography (CT)[9], magnetic resonance imaging (MRI)[10] and positron emission tomography (PET)[11], have demonstrated good performance in understanding the pathological dysfunction of the cerebrovascular system, owing to its unlimited penetration depth.[12] However, most of these imaging models still suffered from morphometric analyses, low spatial resolution and unfavorable imaging sensitivity.[13] Compared with the previously reported imaging method, optical imaging has provided a non-invasive imaging method for studying the cerebral dysfunction or disease, owing to its advantages of high sensitivity, and high spatial/temporal resolution, which plays a major role in both biomedical and clinic diagnostics.[12,13] However, the traditional optical imaging method by using visible and first near-infrared (NIR-I) light still suffer from intrinsic drawbacks, including inevitable tissue scattering, relative low tissue-penetration depth, subsequently leading to a low imaging quality and resolution.[14-23] Therefore, developing optical probe with low scattering losses, high penetration depth, and imaging resolution is highly demanded for vascular imaging.

Recently, optical imaging in short wavelength near-infrared region (1000-1700, referred as NIR-II) has been emerged as the next generation imaging technique for *in vivo* vascular imaging owing to its negligible tissue auto-fluorescence, reduced tissue scattering over NIR-I, and significant improvements in tissue penetration and spatial resolution.[24,25] At present, there are several kinds of materials capable of generating NIR-II emission, such as quantum dots (QDs),[26-32] aggregation-induced emission dots,[33] single-walled carbon nanotubes (SWNTs),[34-41] and small

organic molecular.[42-50] Nevertheless, most of QDs always contain toxic elements, such as lead, or arsenic,[26-29] preventing their widespread bioimaging application *in vivo*. Although NIR-II imaging by using SWNTs has achieved a great progress for non-invasive brain vessel imaging.[1] However, there are still some unavoidable drawbacks, including the broad band emission peaks (>300 nm), low QY (0.1-0.4%), and uniform size distribution, impeding further practical application as NIR-II emitters.[24,51] Small organic molecules usually present high photo-bleaching and rapid clearance from the diseased organs and tumor site, making them unsuitable for tumor diagnosis usually long-term imaging needed.[45] Notably, compared with NIR-II imaging using 1000-1400 nm emission, the 1500-1700 nm (referred as NIR-IIb) emission region is more beneficial for *in vivo* fluorescence imaging with superior imaging quality owing to the low fluorescence signal attenuation by water and the reduced photon scattering[45]. However, highly bright NIR-IIb fluorescent probes with uniformed size and high QY are still rarely explored.

Rare-earth based nanomaterials have been emerged as desirable probes for biological imaging application in the NIR-I region, owing to their advantages of low biotoxicity, high photostability, narrow band emission, and uniform size distribution.[14-23] Notably, among the various Yb/Er-doped host materials, $NaLnF_4$ nanocrystals are commonly regarded as the most efficient UC hosts.[20] However, the relatively low UC emission efficiency and large tissue scattering in NIR-I region impede their wide applications in optical bioimaging. Fortunately, it simultaneously holds high efficient downshifting emission in 1525 nm accomplished with the UC emission, under the excitation of 980 nm laser, featuring the significant reduction in photon scattering than the UC NIR-I/visible region,[24,52-57]. In addition, the downshifting and UC emissions in same host are two competing processes. Recently, Dai's group[52] demonstrated a $NaYbF_4$:Yb/Er@$NaYF_4$ core/shell nanoprobe with enhanced 1525 nm emission *via* Ce^{3+} doping

method for high temporal resolution imaging of brain vessel. However, the NIR-II imaging by using rare earth-based nanoprobe is still in an infant stage.

Herein, we demonstrated a $NaLnF_4$:Gd/Yb/Er fluorescent agent (Ln=Y, Yb, Lu) with enhanced NIR-IIb emission at 1525 nm for small tumor/metastasis tumor diagnosis and non-invasive brain/tumor vascular imaging *via* doping Ce^{3+}. Mentionable, the downshifting emission in 1525 nm was highly enhanced by boosting the downshifting pathway and suppressing the UC emission. *In vivo* optical-guided tumor-related vascular imaging is demonstrated with high resolution. These findings reveal that the explored PAA-Lu-NRs probes with high biocompatible and bright SWIR emission are promising agent for optical-guided non-invasive tumor/brain vascular imaging and small tumor/metastasis tumor diagnosis in the advanced NIR-II window.

Results and Discussion

High quality $NaLnF_4$ luminescent nanorods with boosted NIR-IIb emission and enhanced QY. As shown in **Scheme 1** and **Figure 1a,** the high quality NIR-IIb emitting nanorods with uniform size, improved downshifting emission beyond 1500 nm and QY by using Ce^{3+} doping are demonstrated for optical-guided metastatic tumor diagnosis, tumor and brain vessel imaging. To reveal the effect of Ce^{3+} doping on the crystal structure and size, the $NaLuF_4$ nanocrystals doped with different concentrations of Ce^{3+} were first tested by using a transmission electron microscopy (TEM, Figure 1b-1f) and X-ray powder diffraction (XRD, Figure 1i). Without the presence of Ce^{3+}, the sample presents highly uniform rod-like structure (Figure 1b). And with adding Ce^{3+}, all of the samples still maintain the rod-like shape and size (Figure 1b-1d, 1f). High-resolution TEM (HRTEM, Figure 1e) image of a single nanorod taken from Figure 1d indicates the high crystallization nature with d-spacing of 3.01 Å, matching well the (100) crystal

plane of the hexagonal phase $NaLuF_4$. Moreover, energy dispersive X-ray spectrometer (EDS) analyses (**Figure S1**) taken from Figure 1d also indicate the presence of Na, Lu, F, Gd, Er and the doped Ce elements. To further reveal the element distribution of the $NaLuF_4$: 40Gd/20Yb/2Er/xCe nanorods, we have carried out EDS mapping test. **Figure S2a** shows a scanning TEM (STEM) image of the $NaLuF_4$:40Gd/20Yb/2Er/5%Ce nanorods. As demonstrated, the nanorods present uniform element distribution throughout the detected area. And the element compositions of the $NaLuF_4$: 40Gd/20Yb/2Er/5%Ce nanorods were further tested by using X-ray photoelectron spectroscopy (XPS). As shown in **Figure S3**, XPS results also showed the presence of Ce element in host matrix, further verifying the successful incorporation of Ce^{3+} into the host. Dynamic light scattering (DLS) measurement (**Figure S4)** was performed to evaluate the aggregation degree of the samples, revealing the low aggregation and uniform distribution, which are consistent with TEM results.

To further verify the crystal phase structure of the as-prepared samples, XRD measurements were performed. As shown in Figure 1i, with increasing the Ce concentration, all the samples show the hexagonal phase structure (JCPDS: 27-1427), no other extra peaks are observed, also indicating the formation of pure hexagonal phase structure. And the diffraction peak of (300) crystal plane gradually shift to lower angle from 2θ of 53.34 to 52.94, which is mainly ascribed to the substitution of Lu^{3+} (r=1.117Å)[58] by larger Ce^{3+} (1.283Å)[58]. To reveal the Ce^{3+} doping induced lattice constant change, we have measured the lattice parameters for $NaLuF_4$: Yb/Er/Gd nanorods doped with different Ce^{3+}. As demonstrated in **Table S1**, the lattice parameter is gradually increased by improvement of Ce^{3+} dopant contents. These results indicate that the Ce^{3+} ions are successfully incorporated into the host matrix[59]. For comparison, the different Ce^{3+} doped $NaYbF_4$ and $NaYF_4$ nanorods were also prepared by the same method. As shown in

Figure S5 and Figure 1g and 1h, TEM results reveal that the $NaLnF_4$ (Ln=Yb, Y) nanorods doped with different contents of Ce^{3+} (2% to 10%) show the same highly-uniform rod-like morphology and crystallization in accordance with the case of $NaLuF_4$ nanorods.

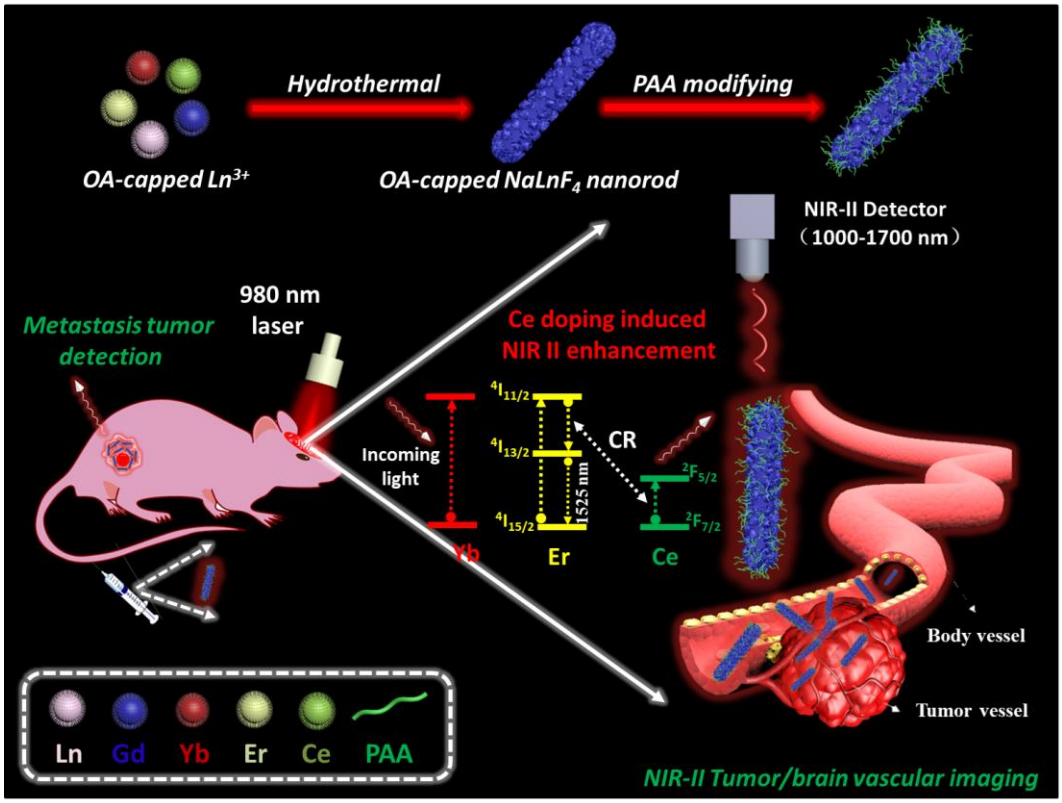

Scheme 1. Schematic illustration of the enhanced NIR-IIb emission of PAA-Ln-NRs *via* Ce^{3+} doping for non-invasive tumor metastasis/vascular visualization and brain vessel imaging.

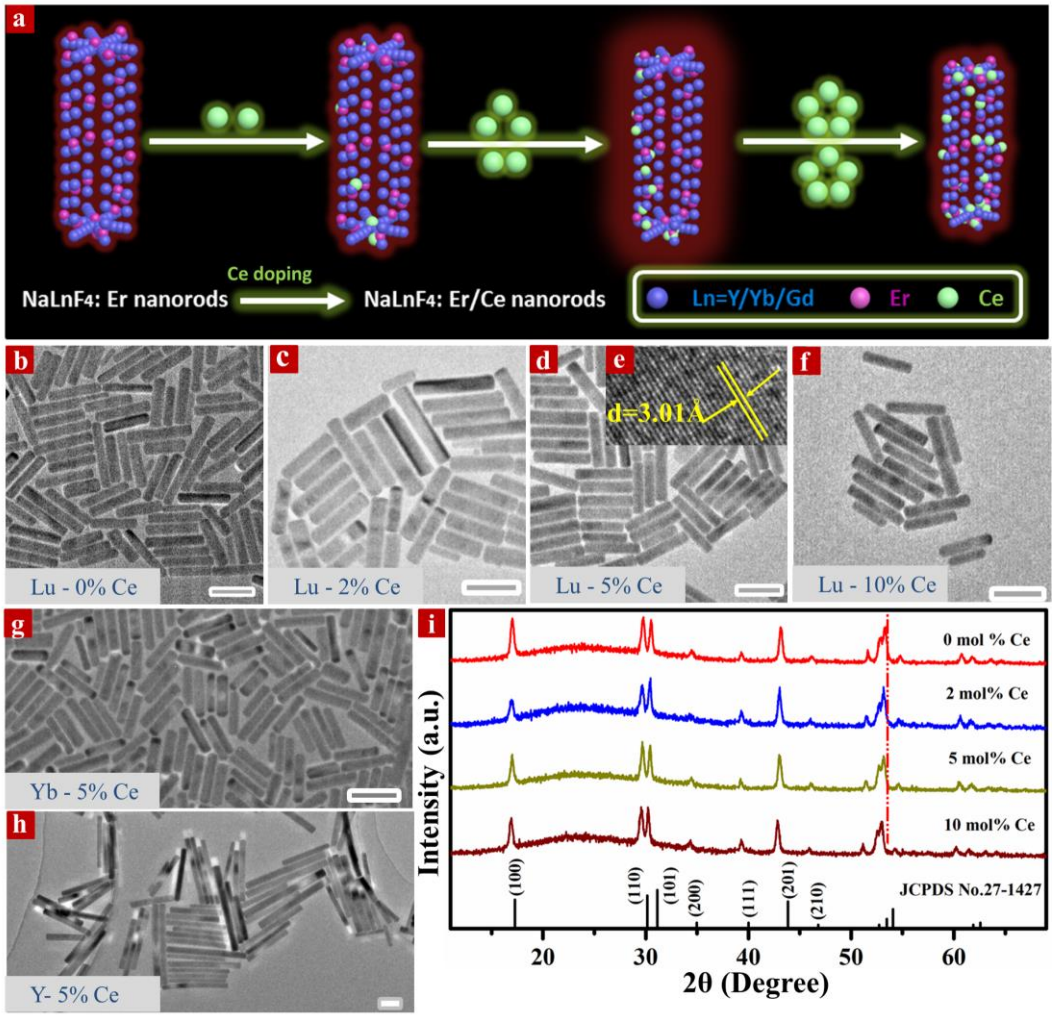

Figure 1. (a) Schematic presentation of the synthesis process of the different Ce^{3+} doped $NaLnF_4$:40Gd/20Yb/2Er nanorods. (b), (c), (d) and (f) TEM images of $NaLuF_4$:Yb/Gd/Er samples doped with different concentrations of Ce^{3+} (0, 2, 5, 10 mol%), respectively. (g) and (h) TEM images of $NaYbF_4$:40Gd/2Er/5%Ce and $NaYF_4$:20Yb/40Gd/2Er/5%Ce samples, respectively. All the scale bars are 100 nm. (e) HRTEM image taken from d. (i) The XRD patterns of the as prepared $NaLuF_4$ samples doped with different concentrations of Ce^{3+} (0, 2, 5, 10 mol%). The red dotted line indicates the diffraction peaks shift to lower angle direction.

To reveal the effect of Ce^{3+} doping on the optical properties, the UC visible and downshifting NIR-IIb spectra of $NaLnF_4$:Yb/Ce/Gd/Er nanorods were systematically studied. As shown in **Figure 2a** and 2e, **Figure S6** and **Figure S7,** all of the samples present two characteristic UC visible emission bands centered at 525/545 and 650 nm and one efficient downshifting NIR-IIb emission centered at 1525 nm. The UC visible emission is mainly ascribed to the efficient energy transfer from Yb^{3+} to Er^{3+} to excite the intermediate $^4I_{11/2}$ state to the higher $^2H_{11/2}$ and $^4S_{3/2}$ energy levels (Figure 2c), finally resulting in the corresponding UC visible emissions. While for simultaneous NIR-IIb emission, a rapid phonon mediated non-radiative decay from $^4I_{11/2}$ to $^4I_{13/2}$ level is occurred for generating 1525 nm downshifting emission[60]. It is noted that both the downshifting and UC emitting processes are all highly related to the intermediate $^4I_{11/2}$ state of Er^{3+}, presenting competitive emission process. Therefore, to achieve high efficient NIR-IIb emission, a suppressed UC emission by decreasing the population of $^4I_{11/2}$ state and simultaneously increasing the electron numbers in $^4I_{13/2}$ level demanded[52,60-62] Fortunately, the energy level difference between $^2F_{5/2}$ and $^2F_{7/2}$ states of Ce^{3+} is about 2300 cm^{-1}, which is approximated to the energy level spacing of $^4I_{11/2}$ and $^4I_{13/2}$ (about 3700 cm^{-1}) of Er^{3+}, enabling phonon-mediated non-radiative decay from $^4I_{11/2}$ to $^4I_{13/2}$ level of Er^{3+} *via* the efficient cross relaxation (CR, Figure 2c) between Er^{3+} ($^4I_{11/2}\rightarrow{}^4I_{13/2}$) and Ce^{3+} ($^2F_{7/2}\rightarrow{}^2F_{5/2}$). Moreover, Dai's group[52] proposed a Ce^{3+} doping strategy to boost the 1525 emission in $NaYbF_4$-based core/shell nanoparticles for high temporal resolution brain vessel imaging. Thus, inspired by Dai's report[52], a general Ce^{3+} doping method is adopted here to improve the downshifting NIR-IIb emission and simultaneously suppressing UC process. As shown in Figure 2b, 2d and 2e, a significant enhancement (200%) of NIR-IIb emission at 1525 nm was realized by doping 5% Ce^{3+} in the $NaLuF_4$ host. Meanwhile, the overall UC emission intensity was dramatically

decreased *via* doping Ce^{3+}, owing to the efficient phonon assistant CR process between Er^{3+} and Ce^{3+}. And further increasing Ce^{3+} contents, the NIR-IIb emission intensity was gradually decreased (Figure 2d and Figure 2e), which is mainly attributed to the concentration quenching effect at a higher Ce doping concentration, revealing a limit depopulation of $^4I_{11/2}$ level of Er^{3+} by Ce^{3+} doping. Additionally, to reveal the effect of Er^{3+} content on the NIR-IIb emission, NIR-IIb emission properties of the $NaLuF_4$:Gd/Yb/5%Ce nanorods doped with different concentrations of Er^{3+} (2%, 10%, 20%) were further studied. As shown in **Figure S8**, the NIR-IIb emission intensity was dramatically decreased (~ 2 times) when increasing Er^{3+} content from 2 to 10%. With further increasing the Er^{3+} dopant content to 20%, the emission intensity was decreased for about 4 times, matching well with the *in vitro* phantom imaging results (inset of Figure S8). These results reveal that the Er dopant content of 2% is an optimal doping content for 1525 nm emission in PAA-Lu-NRs.

Moreover, the NIR-IIb emission intensity of the $NaYbF_4/NaYF_4$ host**s** was also enhanced by 1.75 times and 2.2 times by adjusting the Ce^{3+} contents to 5%, respectively. As a comparison experiment, the NIR-IIb emission properties of 5% Ce doped $NaLnF_4$ (Ln= Lu, Yb, Y) nanorods were further studied. As shown in Figure 2f, 2g and 2h, the Lu-based host showed the most efficient NIR-IIb emission over the three hosts, making it an ideal nanoprobe for NIR-IIb bioimaging. The QY of NIR-IIb emission of $NaLnF_4$:5% Ce nanorods in water was determined in a similar way to the previous report[41] by using a standard IR-26 dye (QY = 0.5%) dissolved in 1,2-dichloroethane (DCE) as a reference. As demonstrated in **Table S2**, Lu-based probes doped with 5% Ce^{3+} present the highest QY in cyclohexane (26 %) and in water (3.6%) among the three Ln-based hosts, which is also relative higher than the previously reported lanthanide probe with QY of 23.1% in hexagonal and 2.73% in water[52] and SWNTs with low QY of 0.4%[55].

Therefore, the Lu-based nanorods hold merits of narrow-band emission (~160 nm), high QY (3.6% in water) and uniform size, making their more competitive probe for further biological application. Prior to *in vivo* imaging, the hydrophobic 5 mol% Ce doped $NaLuF_4$:Yb/Er/Gd nanorods were converted to hydrophilic ones by using a typical PAA-modifying method.[63] The zeta potential of the PAA-Lu-NRs was first tested and revealed the negative charge nature on the surface (-38.4 mV), indicating the successful modification of PAA on the surface of the $NaLuF_4$: 40Gd/20Yb/2Er/5%Ce nanorods. The stability of the PAA-Lu-NRs in phosphate buffer solution (PBS) and fetal bovine serum (FBS) was further studied. As shown in **Figure S9**, the PAA-Lu-NRs solution presents no detectable aggregation in PBS and FBS in 1 day and 7 days, indicating the high stability of this probe for biomedical application.

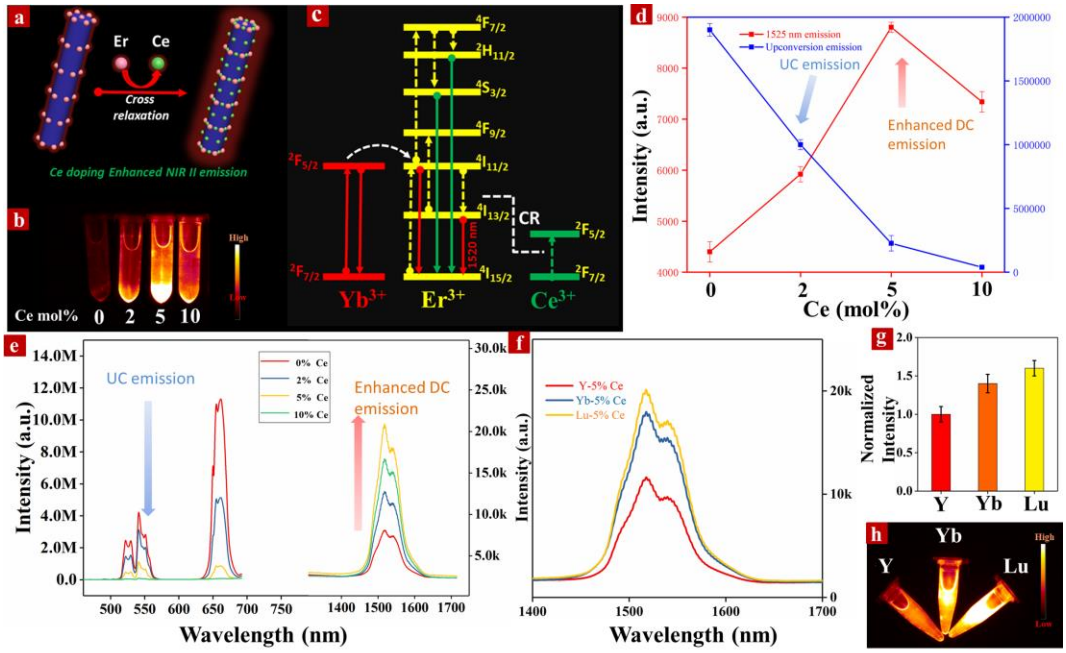

Figure 2. (a) The proposed mechanism of Ce doping-induced NIR-IIb emission enhancement. (b) *In vitro* NIR-IIb fluorescent imaging of $NaLuF_4$:40Gd/20Yb/2Er/X%Ce (X= 0, 2, 5, 10) nanorods under the excitation of 980 nm laser. (c) Simplified energy level diagram

revealing the energy transfer between Yb^{3+}, Er^{3+}, and Ce^{3+} ions. (d) The corresponding UC and NIR-IIb emission intensity evolution under 980 nm excitation. (e) UC and NIR-IIb luminescence spectra of $NaLuF_4$:Gd/Yb/Er nanorods doped with different contents of Ce^{3+} (0, 2, 5, 10 mol%). (f) NIR-IIb luminescence spectra of the $NaLnF_4$:40Gd/20Yb/2Er/5%Ce (Ln=Y, Yb, Lu) nanorods. (g) The corresponding NIR-IIb emission intensity of the $NaLnF_4$:40Gd/20Yb/2Er/5%Ce (Ln=Y, Yb, Lu) nanorods. (h) *In vitro* phantom NIR-IIb fluorescent imaging of $NaLnF_4$:40Gd/20Yb/2Er/5%Ce (Ln=Y, Yb, Lu) nanorods under 980 nm laser excitation.

***In vivo* optical-guided small tumor diagnosis in the NIR-IIb window.** *In vivo* small tumor detection has played a very important role for early cancer diagnosis. However, until now, it is still a great challenge to diagnose the small tumor (below 5 mm) owing to the lower uptake of macromolecular drugs and dramatic comparable geometric resistances.[64] Therefore, an effective nanoparticulate probes with improved accumulation in small tumor is urgently needed. For further assessing the ability of PAA-Lu-NRs for small tumor detection, *in vivo* optical-guided NIR-IIb bioimaging of a tumor-bearing mouse was performed. The *in vivo* NIR-IIb bioimaging (**Figure 3a**) of the tumor-bearing mouse was performed by intravenously injecting a 200 μL PAA-Lu-NRs (3 mg/mL) solution. As demonstrated in Figure 3b, NIR-IIb fluorescent signals were observed in the liver and spleen site of the mouse after 1 h injection. Subsequently, NIR-IIb fluorescent signal in the tumor site was also observed after 24 h injection and gradually enhanced until 48 h injection, revealing the effective accumulation of PAA-Lu-NRs in the tumor site and feasible application for long-time tracking of tumor (Figure 3c). The tumor to normal (T/N) tissue ratio (**Figure S10**) of the mouse was further evaluated, presenting the high T/N ratio of ~16. To reveal the biodistribution of the PAA-Lu-NRs in the living body, the tumor-bearing

mouse was dissected to obtain the isolated organs (liver, heart, spleen, kidneys, lung, and tumor) for further *ex-vivo* NIR-IIb imaging. As shown in Figure 3d, bright NIR-IIb emission can be detected in the liver, spleen, lung and tumor site, indicating the same distribution trend with the living mouse (Figure 3b). Additionally, the quantitative analysis of the fluorescence intensity was performed. As shown in **Figure S11**, the PAA-Lu-NRs were found to mainly accumulated in the liver (34.7%), spleen (39.1%) and lung (17.3%), and tumor site (8%), indicating the efficient tumor uptake of the PAA-Lu-NRs *via* enhanced permeability and retention (EPR) effect.

To further reveal the time-dependent biodistribution of the PAA-Lu-NRs, *in vivo* (**Figure S12)** and *ex vivo* (**Figure S13)** bioimaging of normal mice were performed. As shown in Figure S12 and **Figure S14**, the NIR-IIb signal in the liver of the mouse was gradually enhanced after 12 h injection and subsequently decreased after 24 h injection. *Ex vivo* bioimaging (Figure S13c and d) demonstrated that the optical signals were mainly observed in the liver, spleen and lung organs then gradually enhanced after 12 h injection and decreased after 24 h injection, which was also matched well with the aforementioned results of *in vivo* tumor imaging. The pharmacokinetic behavior (Figure S13a and b) was also evaluated by testing the blood samples at different time points (1 min ~ 24 h), which is similar with the previously reported method.[52] The half-life of the PAA-Lu-NRs in the living mouse was measured to be ~ 76 min. It should be pointed out that the accumulation of nanoprobes in liver and spleen may result in immune response. Thus, to preliminary evaluation of the immune response and biotoxicity, the immune response test (**Table S3)** and weight changes (**Figure S15)** of the normal mice were performed. As shown in **Table S3**, the immune organs index presents no obvious differences between the control and test mice, indicating the low immune response and high biocompatibility of the PAA-Lu-NRs. And, no significant weight change was observed in the control group and treated

group mice, also validating the high biocompatibility of PAA-Lu-NRs for bioimaging application. Therefore, these results imply that the PAA-Lu-NRs are ideal NIR-IIb-emitters for deep tissue bioimaging and small tumor detection.

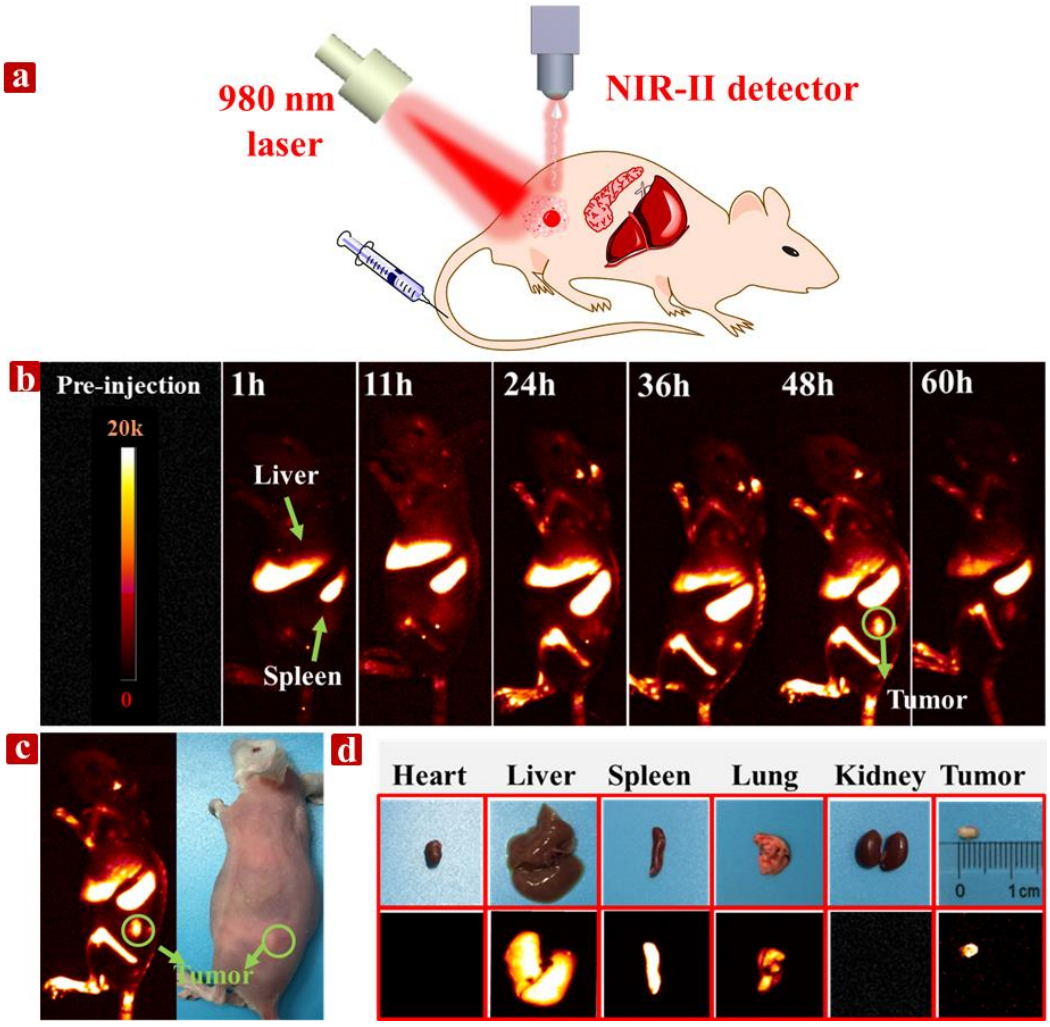

Figure 3. (a) Schematic illustration of *in vivo* small tumor diagnosis by using PAA-Lu-NRs. (b) NIR-IIb bioimaging of LLC tumor-bearing mouse after intravenously injecting PAA-Lu-NRs at different time periods. (c) Digital photograph of tumor-bearing mouse and *in vivo* NIR-IIb fluorescent imaging of the tumor-bearing mouse (the green circle indicated the tumor site). (d) Digital photographs of the isolated organs/tumor and the corresponding *ex-vivo* NIR-IIb imaging,

respectively.

Optical imaging-guided metastatic tumor diagnosis and tumor vessel imaging. Early diagnosis of small tumor is highly important for cancer therapy and improving survival rate.[32] It is well known that the formation and growth of tumor is highly depended on the blood supply around the tumor. Therefore, non-invasive imaging of tumor vessels with high spatial resolution may provide more detailed information on tumor vessel morphology, lengths, and leakage nature[32,46] For further assessing the ability of PAA-Lu-NRs for tiny metastatic tumor detection and tumor vascular imaging, *in vivo* NIR-IIb bioimaging of the Lewis lung carcinoma (LLC) tumor-bearing mouse (primary tumor site labelled in 1) was performed. As shown in **Figure 4a**, after 10 s injection, the PAA-Lu-NRs probes were immediately entered into the systemic blood circulation, resulting in the clear identification of tumor vessels owing to the abundant vessel around the tumor. Then the fluorescence signal was decreased with prolonging the injection time and scarcely observed after 8 min injection. After 24 h injection, the fluorescence signals in the primary tumor site 1 were gradually enhanced, indicating the efficient uptake of PAA-Lu-NRs in the tumor site by EPR effect. And in comparison with the initial injection time (before 8 min), the fluorescence signals were almost observed in the tumor inner region. This is mainly ascribed to the translocation of nanoprobes from systemic blood circulation to tumor interior region *via* EPR effect. More importantly, an extra fluorescence signal in the back of the mouse was observed, which was mainly attributed to the tumor metastasis from site 1 to site 2. To further verify the tumor metastasis, the tumor in site 2 was then dissected, a tiny metastatic tumor (~ 3 mm in diameter, Figure 4b and 4c) was observed. *Ex vivo* NIR-IIb imaging (Figure 4c) of the dissected metastatic tumor in site 2 also demonstrated the presence of fluorescence signal in the metastatic tumor, unambiguously validating the tumor metastasis. It should be pointed out that

the tumor size has a great influence on the uptake of nanoprobes *via* EPR effect. Although, the tiny tumors with size of 1-2 mm have little vasculature and ultra-low EPR effect[65], Gao et al. still demonstrated the efficient uptake of UC nanoparticles in tiny tumor with size of 2 mm *via* EPR effect[64]. And, as demonstrated in Figure 4, our detected metastatic tumor with size of about 3-4 mm also presents some vessels around the tumor, indicating the possible accumulation of nanoprobes in the tiny metastatic tumor through EPR effect, which is also consistent with the results of Figure 3 and Figure S11. Moreover, as shown in Figure 4, the higher NIR-IIb emitting signal after 24h injection was observed than that in the tiny metastatic tumor, further revealing the size dependent EPR effect of the tumor.[66]

It is worth noting that our nanoprobes are non-specifically accumulated in the reticuloendothelial system (RES) such as liver and spleen, potentially resulting in undesirable interference signal for tumor detection. It is known that the non-specific uptake of nanoprobes in RES was regarded as the main issue and major challenge for the delivery of nanoprobes to other targeting sites. Thus, reducing the non-specific accumulation of inorganic nanoprobes in RES renders minimized background interference in the liver and spleen, which is beneficial for highly sensitive diagnosis of primary and metastatic tumors. Therefore, it is significant to developing nanoprobes with low non-specific RES accumulation through coating protein-adsorption resistant ligands or synergistically integrating of the EPR effect with active targeting strategy[66], which is needed for further study.

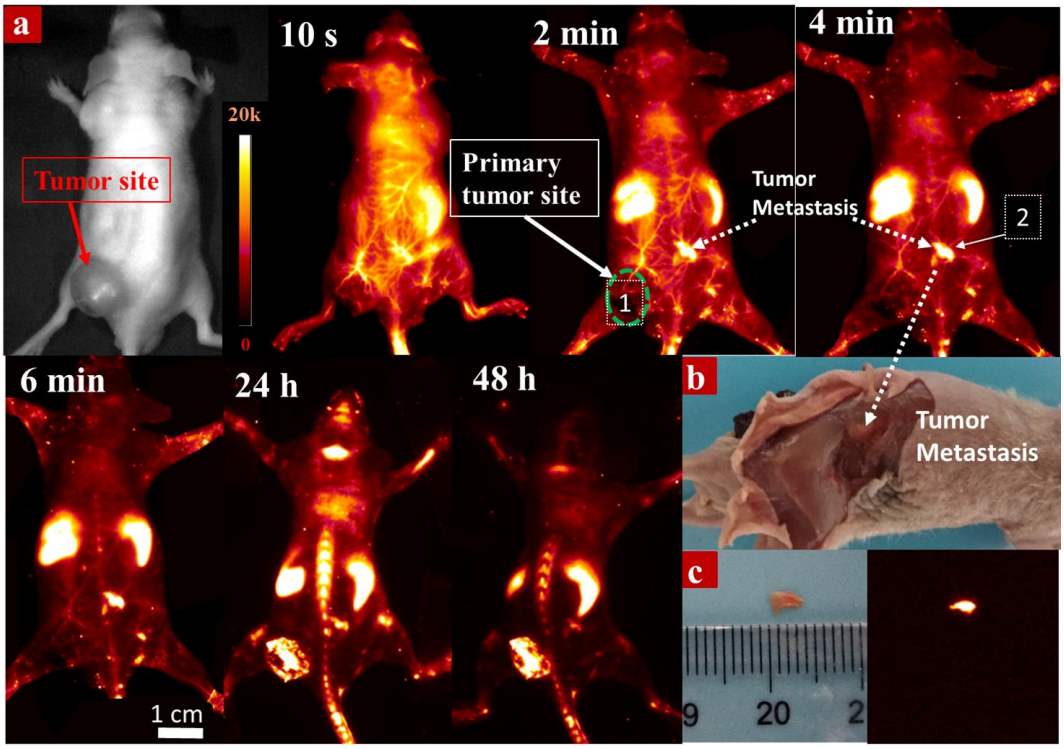

Figure 4. (a) Non-invasive optical imaging-guided tumor metastasis/vessel imaging. Tumor site 1 was the original cultured tumor, tumor site 2 was the metastasis tumor from site 1. (b) *In situ* digital photograph of the LLC tumor-bearing mouse with skin dissected. (c) *Ex vivo* NIR-IIb bioimaging (right panel) and the digital photograph (left panel) of the metastasis tumor.

In addition, high magnification NIR-IIb optical imaging-guided dynamic tumor vessel imaging in primary tumor site 1 with field of view (FOV) of 26 mm×21 mm was further performed. As shown in **Figure 5a**, **5b and 5c**, after intravenous injection of PAA-Lu-NRs solution 10 s, abundant vessels in the tumor site were observed, providing necessary conditions for the tumor growth. The fluorescence signal of the tumor vessel decreased after 8 min injection. To further evaluate tumor vessel visualization, we performed the cross-sectional analysis of the tumor vessel marked by the blue lines. As shown in Figure 5d and 5e, an ultrasmall tumor vessel with a fitted diameter of 41 μm was observed by using the NIR-IIb bioimaging system. Although

there is a tiny necrosis area (marked by white circle) in the epidermis of the primary tumor, appreciable image from abundant blood vessels in and around the tumor site is still evident. Histological analysis of the primary and metastatic tumor was further performed. As presented in **Figure S16**, the histological results demonstrated the same characteristics between the primary and metastasis tumor. Moreover, the TEM micrographs (**Figure S17**) of the primary and metastasis tumor further confirm the location of the PAA-Lu-NRs inside tumor tissues, indicating the efficient accumulation of PAA-Lu-NRs in both primary and metastasis tumor.

To further reveal the tumor vessel imaging, another colorectal tumor model was used for vessel visualization. As shown in **Figure S18**, the abundant tumor vessels were also clearly identified, matching well with the LLC result. *Ex vivo* bioimaging of the resected tumor after 24 h injection was also performed (Figure S18e) and obvious fluorescence signal in tumor site was clearly observed, also verifying the effective accumulation of PAA-Lu-NRs in the tumor site. Histological analysis was performed by using the hematoxylin and eosin (H&E) sections from the control colorectal tumor-bearing mouse (untreated with nanoprobes) and treated tumor-bearing mouse. As illustrated in Figure S18d, no obvious inflammatory lesion was observed in the tumor sites, indicating the good biosafety of PAA-Lu-NRs for tumor vascular imaging. Thereby, the developed PAA-Lu-NRs can be used as efficient NIR-IIb optical nanoprobe for general tumor vessel imaging and tumor metastasis diagnosis. These findings further extend the NIR-IIb emitting rare-earth based nanoprobes for non-invasive real-time tumor metastasis detection, making it promising agent for the potential applications in optical imaging-guided surgery for primary/metastatic tumor dissection.[67]

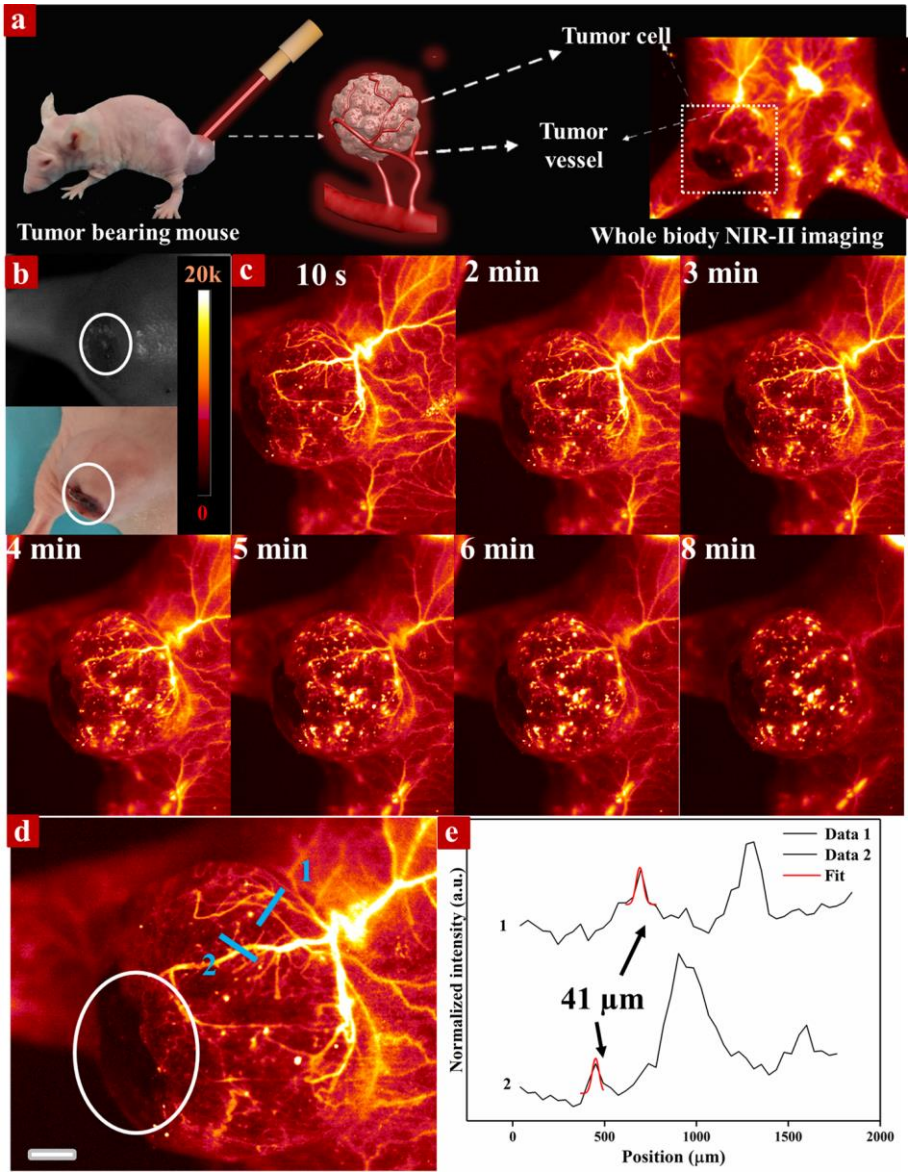

Figure 5. Schematic illustration of NIR-IIb optical imaging-guided LLC vessel imaging. (**b**) A bright field image (up) and digital photograph (down) of LLC tumor. (c) The time coursed NIR-IIb imaging of a mouse tumor under the excitation of 980 nm lase with an excitation power density of 100 mW/ cm^2 (FOV: 26 mm ×21 mm). (d) A magnified tumor vascular image. (e) The cross-sectional fluorescence intensity profiles along blue lines 1 and 2 of the tumor site. The scale bar is 2 mm in (d) and the white circle in (b) and (d) indicates the necrosis region in the epidermis of the primary tumor.

Non-invasive brain vessel imaging. *In vivo* non-invasive imaging of brain vessel has provided an indispensible method for the cerebral dysfunction or brain disease diagnosis.[1] With intravenously injecting PAA-Lu-NRs solution (200 μL, 3 mg/mL) into a Kunming mouse, we performed the non-invasive brain vessel imaging (**Figure 6a**) by using a home-made *in vivo* imaging system[51] equipped with InGaAs detector for 1525 nm emission detection (Princeton Instruments) under 980 nm laser excitation. As shown in Figure 6b, upon injection 8 s later, small cerebral vessels were clearly visualized with excellent spatial resolution. The NIR-IIb signal was slightly decreased after 160 s injection, and almost disappeared within 360 s. This result revealed that the PAA-Lu-NRs with enhanced NIR-IIb emission were promising probe for non-invasive optical-guided brain vessel imaging.

We further demonstrated the cross-sectional analysis of the blood vessel and the fluorescence intensity profiles marked by blue-dashed lines to identify the signal intensity and diameter of the blood vessel. As seen in Figure 6c, the two measurable tiny blood vessels with a fitted diameter of 42 μm (Figure 6d) and 60 μm (Figure 6e) by using Gaussian fits method were distinguished. It is noted that the smallest vessel with full width at half maximum (FWHM) of approximately 42 μm is clearly observed by using the *in vivo* NIR-IIb fluorescence imaging system, which is approximated to the limiting resolution of the current imaging condition with FOV of 26 mm×21 mm (640×512 pixels, 41 μm/pixel). Dynamic NIR-IIb cerebrovascular imaging with high spatial resolution was successfully achieved by using the PAA-Lu-NRs, indicating the feasibility of the PAA-Lu-NRs for brain vascular imaging and early disease prediction and diagnosis. Therefore, it is expected that the NIR-IIb-imaging guided vasculature imaging with high spatial/temporal resolution presented here may have potential applications in

real-time assessment of cerebrovascular anomalies[52], cerebral dysfunction, traumatic brain injury imaging (TBI)[68] and so on.

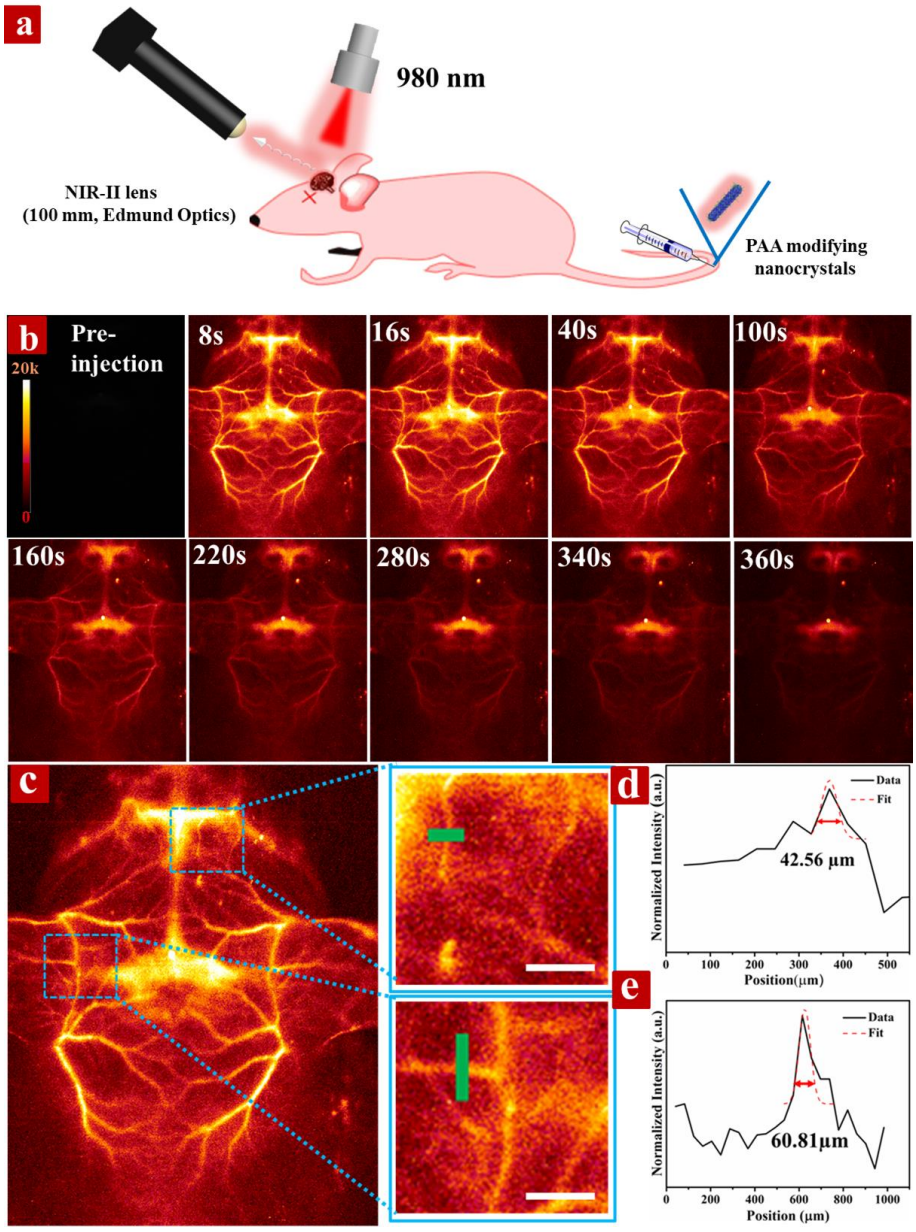

Figure 6. (a) Schematic illustration of *in vivo* non-invasive brain vessel imaging by using the *in vivo* imaging sytem equipped with InGaAs detector (NIR-II lens: 100 mm, Edmund Optics, FOV: 26 mm×21 mm, 640×512 pixels, 41 μm/pixel) and 980 nm laser with an excitation power density of 100 mW/ cm^2 as light source. (**b**) Fast brain vascular imaging of a mouse with hair

removed after injection of 200 μL solution of PAA-Lu-NRs (3 mg/mL) at tail vein under a 980 nm laser excitation. (c) A typical cerebral vascular image and the corresponding zoom-in images of the two blue rectangle areas. (d) and (e) Cross-sectional fluorescence intensity profiles along green lines of the mouse. All the scale bars are 1 mm.

For further evaluating the potential application of PAA-Lu-NRs for fast *in vivo* blood vessel imaging, we also performed the whole body dynamic vessel imaging (FOV: 14.6 cm×18.3 cm) and supine position/prone position (FOV: 26 mm×21 mm, 640×512 pixels, 41 μm/pixel). As shown in **Figure S19a**, the whole body time-dependent dynamic visualization of vessel was achieved. After 4 s injection, bright NIR-IIb fluorescence signal in the small vessel can be observed, and it tends to be decreased after 100 s injection. Finally, the fluorescence signal was scarcely observed after 240 s injection. To further reveal the dynamic visualization of vessel, a high magnification NIR-IIb imaging with FOV of 26 mm×21 mm was performed in supine/prone positions (Figure S19b, Figure S19c). As demonstrated, small vessels were also obviously observed after 4 s injection and decreased after 120 s injection. For further evaluating the high spatial resolution vessel imaging, three peaks in both supine and prone position (**Figure S20 Figure S21**) were identified, and then the Gaussian functions fitting method were used for evaluating the FWHM of the small vessels marked by the white lines. The FWHM of the marked vessels in the prone position (Figure S20b, S20c, S20d) were evaluated to be 42, 58, and 41 μm, respectively. The vessels in the supine position (Figure S21b, S21c, S21d) were 229, 164, and 110 μm, respectively. These results implied the PAA-Lu-NRs are optimum NIR-IIb-emitter for *in vivo* fast vessel tracking.

X-ray bioimaging. Apart from the superior NIR-IIb imaging-guided in-situ tiny metastatic tumor detection, the PAA-Lu-NRs containing Gd element could bring additional imaging

functions such as X-ray and magnetic resonance imaging (MRI), due to the large K-edge value of Lu[69] and efficient intrinsic magnetic moment (μ_{eff}=4.53 μB)[70] of Gd. Therefore, compared with the well-developed SWNTs, NIR-II dyes, and semiconductor nanoparticles, the PAA-Lu-NRs can hold additional imaging ability such as MRI and X-ray imaging.

For revealing the multimodal imaging nature, PAA-Lu-NRs and clinically used iobitridol molecule were used for X-ray bioimaging. As shown in **Figure S22a,** *in vitro* phantom imaging of PAA-Lu-NRs and iobitridol molecules showed concentration-dependent imaging contrast. Moreover, the PAA-Lu-NRs present superior X-ray imaging ability than the iobitridol molecules at the same concentration. And a higher Hounsfield units value of PAA-Lu-NRs (Figure S22b) was achieved, further verifying more efficient X-ray absorption of PAA-Lu-NRs than that of iobitridol molecule. Moreover, *in vivo* CT imaging of mouse after intravenously injecting of PAA-Lu-NRs through tail vein was further performed to assess the feasibility of PAA-Lu-NRs as CT agent. As shown in **Figure S23,** no CT signal was detected in the soft tissues of the mouse without injection of PAA-Lu-NRs solution. And an obvious enhancement of CT signal in the spleen and liver was observed from the top and lateral view of the 3D volume-rendered CT images after 10 min injection. The CT signal gradually increased until 12 h pre-injection and then decreased after 24 h injection, matching well with the *in vivo* and *ex vivo* NIR-II bioimaging results. These results demonstrate that the PAA-Lu-NRs are promising agents for *in vivo* CT imaging.

Histological analysis. Probes with low biotoxicity and high biocompatiblity are highly demanded for biomedicine applications. To reveal this, *in vivo* toxicity evaluation of PAA-Lu-NRs was performed by a typical histological assessment method. **Figure S24** shows the histological analysis of H&E stained organs (heart, liver, spleen, lung and kidney) of the normal

mouse intravenously injected with PAA-Lu-NRs for 3, 7 and 30 days and control group without injection, respectively. No apparent lesions in the isolated organs were observed, indicating the good biocompatibility and negligible toxicity side effect of the PAA-Lu-NRs for biomedical application.

Conclusions

In summary, high quality PAA-Ln-NRs with significantly enhanced downshifting NIR-IIb narrow-band emission beyond 1500 nm, uniformed size, and low bioxoticity *via* Ce^{3+} doping were explored. Optical-guided NIR-IIb small tumor (~4 mm)/metastatic tumor (~3 mm) diagnosis, non-invasive brain vessel imaging and tumor vessel imaging with high spatial resolution (41 μm) are achieved, owing to the strong 1525 nm emission of PAA-Lu-NRs. Therefore, in comparison with SWNTs, the explored PAA-Lu-NRs present highly uniform size, narrow-band emission, high QY (3.6% in water), low toxicity and capacity of multimodal imaging, making it more competitive in the next generation NIR-II optical imaging field.

ASSOCIATED CONTENT

Supporting Information

The Supporting Information is available free of charge on the ACS Publications website.

AUTHOR INFORMATIONs

Corresponding Author

songjunz@hunnu.edu.cn, jh.hao@polyu.edu.hk

ACKNOWLEDGMENT

This work was supported by the National Natural Science Foundation of China (No. 21671064), Science and Technology Planning Project of Hunan Province (No. 2017RS3031).

REFERENCES

(1) Hong, G. S.; Diao, S.; Chang, J. L.; Antaris, A. L.; Chen, C. X.; Zhang, B.; Zhao, S.; Atochin, D. N.; Huang, P. L.; Andreasson, K. I.; Kuo, C. J.; & Dai, H. J. Through-skull fluorescence imaging of the brain in a new near-infrared window. *Nature Photonics* **2014**, *8*, 723-730.

(2) McDonald, D. M. & Choyke, P. L. Imaging of angiogenesis: from microscope to clinic. *Nature Medicine* **2003,** *9*, 713.

(3) Cocker, L. J. D.; Lindenholz, A.; Zwanenburg, J. J.; Kolk, A. V. D.; Zwartbol, M. & Luijten, P.; Hendrikse, J. Clinical vascular imaging in the brain at 7 T. *Neuroimage* **2016**, DOI.10.1016/j. *neuroimage*.2016.11.044.

(4) Wright, S. N.; Kochunov, P.; Mut, F.; Bergamino, M.; Brown, K. M.; Mazziotta, J. C.; Toga, A. W.; Cebral, J. R.; Ascoli, G. A. Digital reconstruction and morphometric analysis of human brain arterial vasculature from magnetic resonance angiography. *NeuroImage* **2013**, *82*, 170-181.

(5) Shlosberg, D.; Benifla, M.; Kaufer, D.; Friedman, A. Blood–brain barrier breakdown as a rapeutic target in traumatic brain injury. *Nature Reviews Neurology*. **2010**, *6*, 393-403.

(6) Frostig, R. D.; Lieke, E. E.; Ts'o, D. Y.; and Grinvald, A. Cortical functional architecture and local coupling between neuronal activity and the microcirculation revealed by *in vivo* high-resolution optical imaging of intrinsic signals. *Proc. Natl. Acad. Sci.USA.* **1990**, *87*, 6082-6086.

(7) Villringer, A. & Chance, B. Non-invasive optical spectroscopy and imaging of human brain function. *Trends. Neuros.* **1997**, *20*, 435-442.

(8) Toi, M.; Asao, Y.; Matsumoto, Y.; Sekiguchi, H.; Yoshikawa, A.; Takada, M.; Kataoka, M.; Endo, T.; Kawaguchi-Sakita, N.; Kawashima, M.; Fakhrejahani, E.; Kanao, S.; Yamaga, I.; Nakayama, Y.; Tokiwa, M.; Torii, M.; Yagi, T.; Sakurai, T.; Togashi K. & Shiina T. Visualization of tumor-related blood vessels in human breast by photoacoustic imaging system with a hemispherical detector array. *Scientific Reports.* **2017**, *7*, 41970.

(9) Schramm, P.; Schellinger, P. D.; Fiebach, J. B.; Heiland, S.; Jansen, O.; Knauth, M.; Hacke, W.; Sartor, K. Comparison of CT and CT Angiography Source Images With Diffusion-Weighted Imaging in Patients With Acute Stroke Within 6 Hours After Onset. *Stroke* **2002**, *33*, 2426-2432.

(10) Jacoby, C.; Boring, Y. C.; Beck, A.; Zernecke, A.; Aurich, V.; Weber, V.; Schrader, J. and Flogel, U. Dynamic changes in murine vessel geometry assessed by high-resolution magnetic resonance angiography: a 9.4T study. *BioTechniques.* **2008**, *28*, 637-645.

(11) Tawakol, A.; Migrino, R. Q.; Bashian, G. G.; Bedri, S.; Vermylen, D.; Cury, R. C.; Yates, D.; LaMuraglia, G. M.; Furie, K.; Houser, S.; Gewirtz, H.; Muller, J. E.; Brady, T. J. L; Fischman, A. G. *In Vivo* ^{18}F-fluorodeoxyglucose positron emission tomography imaging provides a noninvasive measure of carotid plaque inflammation in patients. *Journal of the American College of Cardiology* **2006**, *48*, 1818-1824.

(12) Wang, X. D.; Pang, Y. J.; Ku, G.; Xie, X. Y.; Stoica, G.; Wang, L. H. V. Noninvasive laser-induced photoacoustic tomography for structural and functional *in vivo* imaging of the brain. *Nature Biotechnology* **2003**, *21*, 803-806.

(13) Horton, N. G.; Wang, K.; Kobat, D.; Clark, C. G.; Wise1, F. W.; Schaffer, C. B. and Xu, C. *In vivo* three-photon microscopy of subcortical structures within an intact mouse brain. *Nature Photonics* **2013**, ***7***, 205-209.

(14) Wang, R.; Zhang, F. NIR luminescent nanomaterials for biomedical imaging. *J. Mater. Chem. B* **2014**, *2*, 2422-2443.

(15) Han, S. Y.; Deng, R. R.; Xie, X. J.; Liu, X. G. Enhancing Luminescence in Lanthanide-Doped Upconversion Nanoparticles. *Angew. Chem. Int. Ed*. **2014**, *53*, 11702-11715.

(16) Zhou, J.; Liu, Z.; Li, F. Y. Upconversion nanophosphors for small-animal imaging. *Chem. Soc. Rev*. **2012**, *41*, 1323-1349.

(17) Gai, S. L.; Li, C. X.; Yang, P. P.; Lin, J. Recent progress in rare earth micro/nanocrystals: soft chemical synthesis, luminescent properties, and biomedical applications. *Chem. Rev*. **2014**, *114*, 2343-2389.

(18) Li, X. M.; Zhang, F.; Zhao, D. Y. Lab on upconversion nanoparticles: optical properties and applications engineering *via* designed nanostructure. *Chem. Soc. Rev*. **2012**, *44*, 1346-1378.

(19) Chen, G. Y.; Yang, C. H.; Prasad, P. N. Nanophotonics and nanochemistry: controlling the excitation dynamics for frequency up and down-conversion in lanthanide-doped nanoparticles. *Acc. Chem. Res*. **2013**, *46*, 1474-1486.

(20) Zeng, S. J.; Yi, Z. G.; Lu, W.; Qian, C.; Wang, H. B.; Rao, L.; Zeng, T. M.; Liu, H. R.; Liu, H. J.; Fei, B.; Hao, J. H. Simultaneous realization of phase/size manipulation, upconversion luminescence enhancement, and blood vessel imaging in multifunctional nanoprobes through transition metal Mn^{2+} doping. *Adv. Funct. Mater.* **2014**, *26*, 4051-4059.

(21) Yi, Z. G.; Li, X. L.; Xue, Z. L.; Liang, X.; Lu, W.; Peng, H.; Liu, H. R.; Zeng, S. J. and Hao, J. H. Remarkable NIR enhancement of multifunctional nanoprobes for *in vivo* trimodal bioimaging and upconversion optical/T_2 -weighted MRI-guided small tumor diagnosis. *Adv. Funct. Mater*. **2015**, *25*, 7119-7129.

(22) Pansare, V.; Hejazi, S.; Faenza, W.; Prudhomme, R. K. Review of long-wavelength optical and NIR imaging materials: contrast agents, fluorophores, and multifunctional nanocarriers. *Chem. Mater*. **2012**, *24*, 812-827.

(23) Altınoglu, E. I.; Adair, J. H. Near infrared imaging with nanoparticles. *WIREs Nanomedicine and Nanobiotechnology* **2010**, *2*, 461-477.

(24) Naczynski, D. J.; Tan, M. C.; Tan, M.; Wall, B.; Wall, J.; Kulesa, A.; Chen, S.; Roth, C. M.; Riman, R. E.; Moghe, P. V. Rare-earth-doped biological composites as *in vivo* shortwave infrared reporters. *Nat. Commun*. **2013**, *4*, 2199.

(25) Lim, Y. T.; Kim, S.; Nakayama, A.; Stott, N. E.; Bawendi, M. G.; Frangioni, J. V. Mol. Selection of quantum dot wavelengths for biomedical assays and imaging. *Mol. Imaging.* **2003**. *2*, 50-64.

(26) Hong, G. S.; Robinson, J. T.; Zhang, Y. J.; Diao, S.; Antaris, A. L.; Wang, Q. B.; Dai, H. J. *In vivo* fluorescence imaging with Ag_2S quantum dots in the second near-infrared region. *Angew. Chem. Int. Ed*. **2012**, *51*, 9818-9821.

(27) Zhang, Y.; Hong, G. S.; Zhang, Y. J.; Chen, G. C.; Li, F.; Dai, H. J.; Wang, Q. B. Ag_2S quantum dot: a bright and biocompatible fluorescent nanoprobe in the second near-Infrared window. *ACS Nano* **2012**, *6*, 3695-3702.

(28) Chen, J.; Kong, Y. F.; Fang, H. W.; Wo, Y.; Zhou, D. J.; Wu, Z. Y.; Li, Y. X.; Chen, S. Y. Direct water-phase synthesis of lead sulfide quantum dots encapsulated by β-lactoglobulin for *in vivo* second near infrared window imaging with reduced toxicity. *Chem. Commun.* **2016**, *52*, 4025-4028.

(29) Dong, B. H.; Li, C. Y.; Chen, C. C.; Zhang, Y. J.; Zhang, Y.; Deng, M. J.; Wang, Q. B. Facile synthesis of highly photoluminescent Ag_2Se quantum dots as a new fluorescent probe in the second near-infrared window for *in vivo* imaging. *Chem. Mater*. **2013**, *25*, 2503-2509.

(30) Bruns, O. T.; Bischof, T. S.; Harris, D. K.; Franke, D.; Shi, Y.; Riedemann, L.; Bartelt, A.; Jaworski, F. B.; Carr, J. A.; Rowlands, C. J.; Wilson, M. W. B.; Chen, O.; Wei, H. G.; wang, G. W.; Montana, D. M.; Coropceanu, I.; Achorn, O. B.; Kloepper, J.; Heeren, J.; So, P. T. C.; Fukumura, D.; Jensen, K. F.; Jain, R. K.; Bawendi, M. G. Next-generation *in vivo*

Ioptical imaging with short-wave infrared quantum dots. *Nature Biomedical Engineering*. **2017**, *1*, 0056.

(31) Franke, D.; Harris, D. K.; Chen, O.; Bruns, O. T.; Carr, J. A.; Wilson, M. W. B.; Bawendi, M. G. Continuous injection synthesis of indium arsenide quantum dots emissive in the short-wavelength infrared. *Nat. Comm.* **2016**, *7*, 12749.

(32) Zhang, M. X.; Yue, J. Y.; Cui, R.; Ma, Z. R.; Wan, H.; Wang, F. F.; Zhu, S. J.; Zhou, Y.; Kuang, Y.; Zhong, Y. T.; Pang, D. W.; and Dai, H. J. Bright quantum dots emitting at ~1,600 nm in the NIR-IIb window for deep tissue fluorescence imaging. *Proc. Natl. Acad. Sci. USA* **2018**, *115*, 6590-6595.

(33) Qi, J.; Sun, C. W.; Zebibula, A.; Zhang, H. Q.; Kwok, R. T. K.; Zhao, X. Y.; Wang, X.; Lam, J. W. Y.; Qian, J.; Tang, B. Z. Real-time and high-resolution bioimaging with bright aggregation-induced emission dots in short-wave infrared region. *Adv. Mater.* **2018**, *30*, 1706856.

(34) Welsher, K.; Liu, Z.; Sherlock, S. P.; Robinson, J. T.; Chen, Z.; Daranciang, D.; Dai, H. J. A route to brightly fluorescent carbon nanotubes for near-infrared imaging in mice. *Nat. Nanotechnol.* **2009**, *4*, 773-780.

(35) Robinson, J. T.; Welsher, K.; Tabakman, S. M.; Sherlock, S. P.; Wang, H.; Luong, R.; Dai, H. J. High performance *in vivo* near-IR (>1 μm) imaging and photo thermal cancer therapy with carbon nanotubes. *Nano Res.* **2010**, *3*, 779-793.

(36) Welsher, K.; Sherlock, S. P.; Dai, H. J. Deep-tissue anatomical imaging of mice using carbon nanotube fluorophores in the second near-infrared window. *Proc. Natl. Acad. Sci. USA.* **2011**, *108*, 8943-8948.

(37) Yi, H.; Ghosh, D.; Ham, M. H.; Qi, J.; Barone, P. W.; Strano, M. S.; Belcher, A. M. M13 phage-functionalized single-walled carbon nanotubes as nanoprobes for second near-infrared window fluorescence imaging of targeted tumors. *Nano Lett*. **2012**, *12*, 1176-1183.

(38) Robinson, J. T.; Hong, G. S; Liang, Y. Y; Zhang, B.; Yaghi, O. K.; Yaghi, H. Dai, H. J. *In vivo* fluorescence imaging in the second near-infrared window with long circulating carbon nanotubes capable of ultrahigh tumor uptake. *J. Am. Chem. Soc.* **2012**, *134*, 10664-10669.

(39) Diao, S.; Hong, G. S.; Robinson, J. T.; Jiao, L. Y.; Antaris, A. L.; Wu, J. Z.; Choi, C. L.; Dai, H. J. Chirality enriched (12,1) and (11,3) single-walled carbon nanotubes for biological imaging. *J. Am. Chem. Soc.* **2012**, *134*, 16971-16974.

(40) Hong, G. S.; Lee, J. C.; Robinson, J. T.; Raaz, U.; Xie, L.; Huang, N. F.; Cooke, J. P. & Dai, H. J. Multifunctional *in vivo* vascular imaging using near-infrared II fluorescence. *Nat. Med.* **2012**, *18*, 1841-1846.

(41) Antaris, A. L.; Robinson, J. T.; Yaghi, O. K.; Hong, G.; Diao, S.; Luong, R.; Dai, H. J. Ultra-low doses of chirality sorted (6,5) carbon nanotubes for simultaneous tumor imaging and photothermal therapy. *ACS Nano* **2013**, *7*, 3644-3652.

(42) Sun, Y.; Ding, M. M.; Zeng, X. D.; Xiao, Y. L.; Wu, H. P.; Zhou, H.; Ding, B. B.; Qu, C. R.; Hou, W.; Er-bu, AGA.; Zhang, Y. J.; Cheng, Z.; Hong, X. C. Novel bright-emission small-

molecule NIR-II fluorophores for *in vivo* tumor imaging and image-guided surgery. *Chemical Science* **2017**, *8*, 3489-3493.

(43) Antaris, A. L.; Chen, H.; Diao, S.; Ma, Z. R.; Zhang, Z.; Zhu, S. J.; Wang, J.; Lozano, A. X.; Fan, Q. L.; Chew, L. L.; Zhu, M.; Cheng, K.; Hong, X. C.; Dai, H. J.; Cheng, Z. A high quantum yield molecule-protein complex fluorophore for near-infrared II imaging. *Nat. Commun.* **2017**, *8*, 15269.

(44) Antairs, A. L.; Chen, H.; Cheng, K.; Sun, Y.; Hong, G. S.; Qu, C. R.; Qu, S.; Deng, Z. X.; Hu, X. M.; Zhang, B.; Zhang, X. D.; Yaghi, O. K.; Alamparambil, Z. R.; Hong, X. C.; Cheng, Z.; Dai, H. J. A small-molecule dye for NIR-II imaging. *Nature Materials* **2016**, *15*, 235-242.

(45) Diao, S.; Blackburn, J. L.; Hong, G. S.; Antaris, A. L.; Chang, J. L.; Wu, J. Z.; Zhang, b.; Cheng, K.; Kuo, C. J.; Dai, H. J. Fluorescence imaging i*n vivo* at wavelengths beyond 1500 nm. *Angew. Chem. Int. Ed.* **2015**, *127*, 14971-14975.

(46) Shou, K. Q.; Qu, C. R.; Sun, Y.; Chen, H.; Chen, S.; Zhang, L.; Xu, H. B.; Hong, X. C.; Yu, A.; Cheng, Z. Multifunctional biomedical imaging in physiological and pathological conditions using a NIR-II Probe. *Adv. Funct. Mater.* **2017**, *27*, 1700995.

(47) Yang, Q. L.; Ma, Z. R,; Wang, H. S.; Zhou, B.; S. Zhu, J.; Zhong, Y. T.; Wang, J. Y.; Wan, H.; Antaris, A.; Ma, R.; Zhang, X.; Yang, J. Y.; Zhang, X. D.; Sun, H. T.; Liu, W. Q.; Liang, Y. Y.; Dai, H. J. Rational design of molecular fluorophores for biological imaging in the NIR-II window. *Adv. Mater.* **2017**, 29, 1605497.

(48) Wang, W. Z.; Ma, Z. R.; Zhu, S. J.; Wan, H.; Yue, J. Y.; Ma, H. L.; Ma, R.; Yang, Q. L.; Wang, Z. H.; Li, Q.; Qian, Y. X.; Yue, C. Y.; Wang, Y. H.; Fan, L. Y.; Zhong, Y. T.; Zhou, Y.; Gao, H. P.; Ruan, J. S.; Hu, Z. Y.; Liang, Y. Y.; Dai, H. J. Molecular cancer imaging in the second near-infrared window using a renal-excreted NIR-II fluorophore-peptide probe. *Adv. Mater*. **2018**, *30***,** 1800106.

(49) Hong, G. S.; Zou, Y. P.; Antaris, A. L.; Diao, S.; Wu, D.; Cheng, K.; Zhang, X. D.; Chen, X.; Liu, B.; He, Y. H.; Wu, J. Z.; Yuan, J.; Zhang, B.; Tao, Z. M.; Fukunaga, C & Dai, H. J. Ultrafast fluorescence imaging *in vivo* with conjugated polymer fluorophores in the second near-infrared window. *Nat. Commun.* **2014**, *5*, 4206.

(50) Zhu, S. J.; Yang, Q. L.; Antaris, A. L.; Yue, J. Y.; Ma, Z. R.; Wang, H. S.; Huang, W.; Wan, H.; Wang, J.; Diao, S.; Zhang, B.; Li, X. Y.; Zhong, Y. T.; Yu, K.; Hong, G. S.; Luo, J.; Liang, Y. Y.; and Dai, H. J. Molecular imaging of biological systems with a clickable dye in the broad 800- to 1,700-nm near-infrared window". *Proc. Natl. Acad. Sci. USA.* **2017**, *114*, 962-967.

(51) Liu, Z.; Cai, W.; He, L.; Nakayama, N.; Chen, K.; Sun, X.; Chen, X.; Dai, H. J. *In vivo* biodistribution and highly efficient tumour targeting of carbon nanotubes in mice. *Nat. Nanotechnol.* **2006**, 2, 47-52.

(52) Zhong, Y. T.; Ma, Z. R.; Zhu, S. J.; Yue, J. Y.; Zhang, M. X.; Antaris, A. L.; Yuan, J.; R. Cui, Wan, H.; Zhou, Y.; Wang, W. Z.; Huang, N. G. F; . Luo, J.; Hu, Z. Y.; Dai, H. J. Boosting the down-shifting luminescence of rare- earth nanocrystals for biological imaging beyond 1500 nm, *Nat. Commun*. **2017**, *8*, 737.

(53) Wang, R.; Li, X. M.; Zhou, L.; Zhang, F. Epitaxial seeded growth of rare-earth nanocrystals with efficient 800 nm near-infrared to 1525 nm short-wavelength infrared downconversion photoluminescence for *in vivo* bioimaging. *Angew. Chem. Int. Ed.* **2014**, *53*, 12086-12090.

(54) Xue, Z. L.; Zeng, S. J.; Hao. J. H. Non-invasive through-skull brain vascular imaging and small tumor diagnosis based on NIR-II emissive lanthanide nanoprobes beyond 1500 nm. *Biomaterials*, **2018**, *171*, 153-163.

(55) Hong, G. S.; Antaris, A. L. and Dai, H. J. Near-infrared fluorophores for biomedical imaging. *Nature Biomedical Engineering* **2017**, *10*, 1-22.

(56) Wang, D.; Wang, D. P.; Kuzmin, A.; Pliss, A.; Shao, W.; Xia, J.; Qu, J. L.; Prasad, P. N. ICG-sensitized $NaYF_4$:Er nanostructure for theranostics. *Adv. Optical Mater*. **2018**, 1701142.

(57) Liu, L.; Wang, S. F.; Zhao, B. Z.; Pei, P.; Fan, Y.; Li, X. M.; Zhang, F. Er^{3+} sensitized 1530 nm to 1180 nm second near-infrared window upconversion nanocrystals for *in vivo* biosensing. *Angew. Chem. Int. Ed.*, **2018**, *57*, 7518-7522.

(58) Shannon, R. D. Revised effective ionic radii and systematic studies of interatomic distances in halides and chalcogenides. *Acta Crystallogr. A* **1976**, *32*, 751-767.

(59) Wang, F.; Han, Y.; Lim, C. S.; Lu, Y. H.; Wang, J.; Xu, J.; Chen, H. Y.; Zhang, C.; Hong, M. H.; Liu, X. G. Simultaneous phase and size control of upconversion nanocrystals through lanthanide doping. *Nature* **2010**, *463*, 1061-1065.

(60) Zhao, X. Y.; Tan, M. C. Ce dopant effects on $NaYF_4$ particle morphology and optical properties. *J. Mater. Chem. C*, **2015**, *3*, 10207-10214.

(61) Jarman, R. H.; Wallenberg, A. J.; Bennett, K. W. & Anthon, D. W. Effects of cerium doping on energy transfer in Yb, Er lasers. *OSA Proc. On Adv. Solid-State Lasers* **1994**, *20*, 160.

(62) Huang, B.; Zhou, Y. X.; Yang, F. J.; Wu, L. B.; Qi, Y. W.; Li, J. The 1.53 μm spectroscopic properties of $Er^{3+}/Ce^{3+}/Yb^{3+}$ tri-doped tellurite glasses containing silver nanoparticles. *Opt. Mater.* **2016**, *51*, 9.

(63) Zhang, T. R.; Ge, J. P.; Hu, Y. X. and Yin, Y. D. A general approach for transferring hydrophobic nanocrystals into water. *Nano Lett*., **2007**, *7*, 3203-3207.

(64) Liu, C. Y.; Gao, Z. Y.; Zeng, J. F.; Hou, Y.; Fang, F.; Li, Y. L.; Qiao, R. R.; Shen, L.; Lei, H.; Yang, W. S.; Gao, M. Y. Magnetic/upconversion fluorescent $NaGdF_4$:Yb,Er nanoparticle-based dual-modal molecular probes for imaging tiny tumors *in vivo*. *ACS Nano* **2013**, *7*, 7227-7240.

(65) Adiseshaiah, P. P.; Hall, J. B.; McNeil, S. E. Nanomaterial standards for efficacy and toxicity assessment. *WIREs Nanomed Nanobiotechnol*, **2009**, *2*, 99-112.

(66) Yu, M. X.; Zheng, J. Clearance pathways and tumor targeting of imaging nanoparticles. *ACS Nano*, **2015**, *9*, 6655-6674.

(67) Wang, P. Y.; Fan, Y.; Lu, L. F.; Liu, L.; Fan, L. L.; Zhao, M. Y.; Xie, Y.; Xu, C. J.; and Zhang, F. NIR-II nanoprobes *in-vivo* assembly to improve image-guided surgery for mnetastatic ovarian cancer. *Nat. Commun*., **2018**, *9*, 2898.

(68) Zhang, X. D.; Wang, H. S.; Antaris, A. L.; Li, L. L.; Diao, S.; Ma, R.; Nguyen, A.; Hong, G. S.; Ma, Z. R.; Wang, J.; Zhu, S. J.; Castellano, J. M.; Wyss-coray, T.; Liang, Y. Y.; Luo, J.; Dai, H. J. Traumatic brain injury imaging in the second near-infrared window with a molecular fuorophore. *Adv. Mater.* **2016**, *28*, 6872-6879.

(69) Liu, Y, L; Ai, K. L.; Liu, J. H.; Yuan, Q. H; He, Y. Y.; Lu, L. H. A high-performance ytterbium based nanoparticulate contrast agent for *in vivo* x-ray computed tomography imaging. *Angew. Chem. Int. Ed*. **2012**, *51*, 1437-1442.

(70) Viswanathan, S.; Kovacs, Z.; Green, K. N.; Ratnakar, S. J.; Sherry, A. D. Alternatives to gadolinium-based metal chelates for magnetic resonance imaging. *Chem. Rev.*, **2010**, *110*, 2960-3018.